Chemical Science

ROYAL SOCIETY OF CHEMISTRY

EDGE ARTICLE

View Article Online
View Journal

Cite this: DOI: 10.1039/d6sc01038e

All publication charges for this article have been paid for by the Royal Society of Chemistry

Received 5th February 2026
Accepted 11th May 2026

DOI: 10.1039/d6sc01038e

rsc.li/chemical-science

Mechanochemically assembled organometallic complexes: a mechanistic study

Lama Hamdouna,[ab] Gianmarco Pisanò,[a] Andrew G. M. Rankin,[c] Julien Trébosc,[c] Laura Falivene,[d] Ida Ritacco,[d] Olivier Devos,[e] Laurent Delevoye,[b] Pascal Roussel,[b] Lucia Caporaso,[d] Luigi Cavallo,[f] Steven P. Nolan,[a] Olivier Lafon *[b] and Catherine S. J. Cazin *[a]

A combination of mechanical synthesis, solid-state analytical techniques (ssNMR, powder XRD, ATR-FTIR) and DFT calculations sheds light on the mechanisms operating in two organometallic solid-state syntheses and highlight the importance of workup protocols in mechanochemical syntheses. The data clearly indicate that product formation can occur during or post grinding.

Introduction

The use of mechanochemical methodologies to carry out chemical transformations of solid reactants is experiencing a period of great activity,[1,2] with numerous applications being reported in a variety of areas of chemical science: organic,[3,4] organometallic,[5,6] main group,[7] and supramolecular chemistry,[8] as well as their uses in metal-mediated,[9] and enzymatic-mediated[10] transformations. The ability to provide a reaction environment devoid of solvents has offered the opportunity to tackle a major problem in the environmental efficiency of synthetic routes: the preponderant issue of solvent waste management.[11] Mechanochemical conditions are generally characterized by higher yields and shorter reaction times when compared to their solution phase incarnations,[12] and have resulted in opportunities to access products otherwise inaccessible by normal solvent-based methodologies[13] (*e.g.*, by eliminating issues associated with solubility of starting materials).[14] Despite its simplicity, the outcome of a mechanochemical reaction involving the treatment of only solid reactants is still difficult to predict *a priori* and there is no established consensus as to what really is a reaction occurring through mechanochemical means alone.[15,16] Hanusa and co-workers have recently reported on how the interaction with the solvent during the workup phase of the synthesis by ball-milling of an allyl calciate species altered the structural arrangement of the final product to its more thermodynamically stable form, and underlined how compounds produced under "dry" milling conditions "undergo a type of selection by solution".[17] Therefore, the understanding of mechanochemical reaction mechanism requires the characterization of the structure of chemical species in the solid state, prior to workup. The most employed characterization techniques for that purpose are powder X-ray diffraction (XRD) and vibrational spectroscopy.[18] Nevertheless, a limited number of studies have recently demonstrated the potential of solid-state nuclear magnetic resonance spectroscopy (ssNMR) to monitor mechanochemical reactions.[19–23] This technique is advantageous since it is quantitative and permits the observation of disordered or amorphous solids.

Herein, we investigate the mechanochemical synthesis of organometallic complexes of Cu(I) and Rh(I) bearing N-heterocyclic carbene (NHC) ligands by combining results from various analytical techniques, including attenuated total reflectance infrared (ATR-FTIR) and ssNMR spectroscopies as well as powder XRD, with density functional theory (DFT) calculations. This project is part of recent efforts by our groups to investigate and exploit the so-called weak base route for the assembly of well-defined transition metal complexes bearing N-heterocyclic carbene (NHC) ligands, using both solution-based and mechanochemical methodologies.[24] The goal of this study is to probe the reaction mechanism leading to the formation of NHC complexes in the solid state, and to understand the sequence of events leading to product formation.

As an initial system to probe mechanochemical reaction mechanism, we have targeted a classically studied copper-NHC based system. Among the various synthetic strategies leading to these complexes, the mechanochemical weak base approach to transition metal-NHC complexes reported concomitantly in

[a]Department of Chemistry and Centre for Sustainable Chemistry, Ghent University, Krijgslaan 289 - S3, 9000 Ghent, Belgium. E-mail: catherine.cazin@ugent.be

[b]Univ. Lille, CNRS, Centrale Lille, Univ. Artois, UMR 8181-UCCS-Unité de Catalyse et Chimie du Solide, 59000 Lille, France

[c]Univ. Lille, CNRS, INRAE, Centrale Lille, Univ. Artois, FR2638 - IMEC – Fédération Chevreul, 59000 Lille, France

[d]Department of Chemistry and Biology, University of Salerno, Via Papa Giovanni Paolo II 132, 84084 Fisciano (SA), Italy

[e]Université Lille, CNRS, UMR 8516, Laboratoire Avancé de Spectroscopie pour les Intéractions la Réactivité et l'Environnement (LASIRE), Lille, France

[f]KAUST Catalysis Center, Physical Sciences and Engineering Division, King Abdullah University of Science and Technology, 23955-6900 Thuwal, Saudi Arabia

2020 by the Cazin and Udvardy groups stands out not only as it employs readily available starting materials in an operationally simple way and makes use of an inexpensive base (*e.g.*, K_2CO_3, Cs_2CO_3) but also because of its wide applicability to different metal centers (*i.e.*, Cu(I), Ag(I), Au(I), Rh(I), Pd(II)),[25–27] in combination with a variety of NHC ligands [benzimidazolium, imidazol(in)ium,[25–27] as well as cyclic (alkyl)(amino)carbene (CAAC)] (Scheme 1).[28] A second system we recently studied also uses the weak base route to produce [Rh(acac)(CO)(NHC)]. In all known cases, however, mechanical treatment of the solid reactants was followed by the subsequent addition of solvents for the workup and purification of the products, and/or the processed samples were dissolved in solvents for characterization. Consequently, little evidence is available to confirm that the observed reactions occur during the mechanical event or because of any follow-up treatment. We now provide evidence for two possible reaction mechanisms involved in mechanochemical reactions: one that is in-line with the reaction occurring because of mechanochemical grinding and a second, that proceeds to product post-grinding after the workup.

Results and discussion

The goal of the initial phase of the present study was to elucidate the mechanism operating in the weak base approach applied to the mechanical synthesis of [Cu(Cl)(NHC)] complexes (Scheme 2), as previously investigated.[26] We hypothesized that the [Cu(Cl)(NHC)] complex is generated through the formation of a cuprate intermediate, drawing upon prior mechanistic studies on the solution-based weak base approach and the isolation of such species.[29] We therefore investigated whether (1) these complexes and cuprate intermediates are formed in the solid state during the ball milling process or during the subsequent workup and (2) whether the final neutral complex formed purely based on the mechanochemical treatment (Scheme 3).[30] For this purpose, we employed ssNMR analysis to monitor the reaction. The imidazolium salt IPr·HCl **1** (IPr = *N*,*N*′-bis-[2,6-(di-iso-propyl)phenyl]imidazol-2-ylidene), was selected as a model substrate and the corresponding [Cu(Cl)(IPr)] complex was obtained in two different ways: (i) one-step one-pot (OP) synthesis and (ii) stepwise (SW) synthesis (Scheme 3).

Proton and ^{13}C solid-state NMR experiments at B_0 = 9.4, 18.8, and 28.2 T, *i.e.*, ^1H Larmor frequencies of 400, 800, and 1200 MHz, respectively, were conducted to monitor the disappearance of the reactants and the formation of the intermediate and final product for the different synthetic routes and workup protocols (Scheme 2).

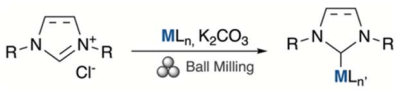

Scheme 1 General weak base approach toward the mechanochemical synthesis of transition metal-NHC complexes.[25]

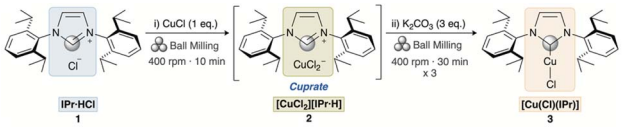

Scheme 2 Weak base approach towards the mechanochemical synthesis of [Cu(Cl)(IPr)].[29] The gray circle denotes the $^{13}C^2$ carbon of the imidazolylidene moiety.

Solid-state NMR spectroscopy

^{1}H ssNMR spectroscopy. The one-dimensional (1D) ^1H solid-state NMR spectra of **1**, **2**, $\mathbf{3^{OP}}$, and $\mathbf{3^{SW}}$ were acquired at a static magnetic field B_0 = 18.8 T, with magic-angle spinning (MAS) frequency ν_R = 60 kHz, to enhance the spectral resolution (Fig. 1). The ^1H signals were assigned (see spectra acquired at B_0 = 28.2 T in Fig. S1) based on ^1H isotropic chemical shifts measured in solution as well as two-dimensional (2D) ^1H–^{13}C heteronuclear correlation (HETCOR) spectra (see Fig. S5), and DFT calculations of ^1H isotropic chemical shifts for periodic crystal structures (see Fig. S2 and Table S1). The H2 imidazolium signal (that bonded to the C2 carbon of the imidazolium) is a good probe of reaction progress since, in Fig. 1a, it is shifted from 12.5 ppm in **1** down to 10 ppm in **2**, whereas it is no longer observed in the ^1H spectra of $\mathbf{3^{SW/OP}}$ owing to the deprotonation of this site.

After 10 min ball milling of [IPr·HCl] in the presence of CuCl, the H2 signal of [$CuCl_2$][IPr·H] cuprate is detected in the

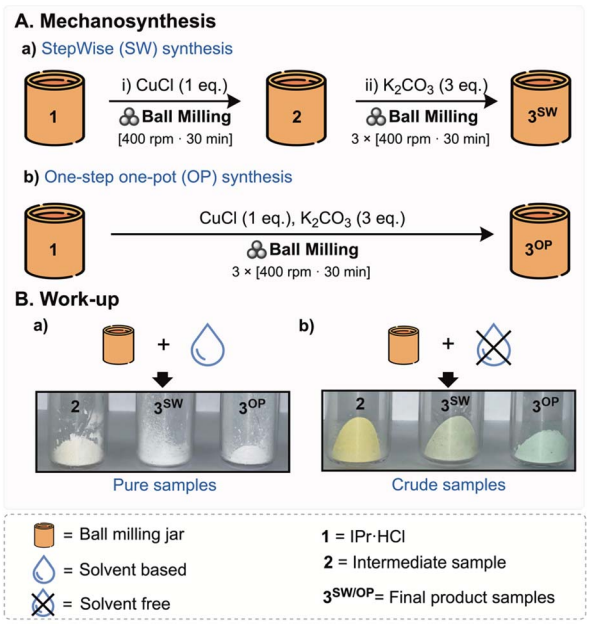

Scheme 3 (A) Schematic outline of the mechanosynthesis: (a) stepwise (SW) synthesis and (b) one-step one-pot (OP) synthesis. (B) Purified and crude samples collected after (a) solvent-based and (b) solvent-free workup procedures. The noticeable colour difference between the crude and purified compounds results from variations in the quantities of unreacted reactants present in the crude mixtures, as verified by the absorbance and luminescence spectra (see Fig. S8).

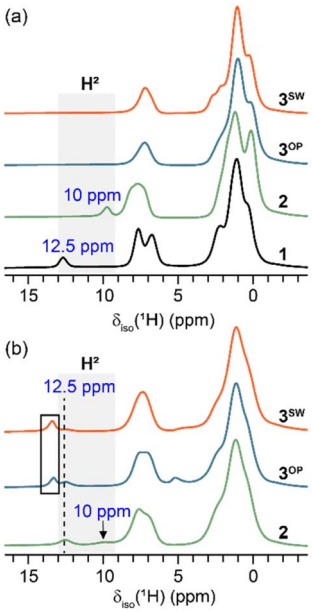

Fig. 1 1D ^{1}H MAS NMR spectra of (a) purified and (b) crude **2** (green), $\mathbf{3}^{OP}$ (blue), and $\mathbf{3}^{SW}$ (orange) acquired at B_0 = 18.8 T with a MAS frequency, ν_R = 60 kHz. The spectrum of **1** compound is also shown in black in panel (a) for the sake of comparison. The shaded area denotes the region where the H2 signal of the **1** and **2** compounds resonates. The ^{1}H signal denoted by the black box in panel b corresponds to $KHCO_3$. The signal resonating near 5 ppm in 1D ^{1}H NMR spectrum of crude $\mathbf{3}^{OP}$ and $\mathbf{3}^{SW}$ is assigned to water.

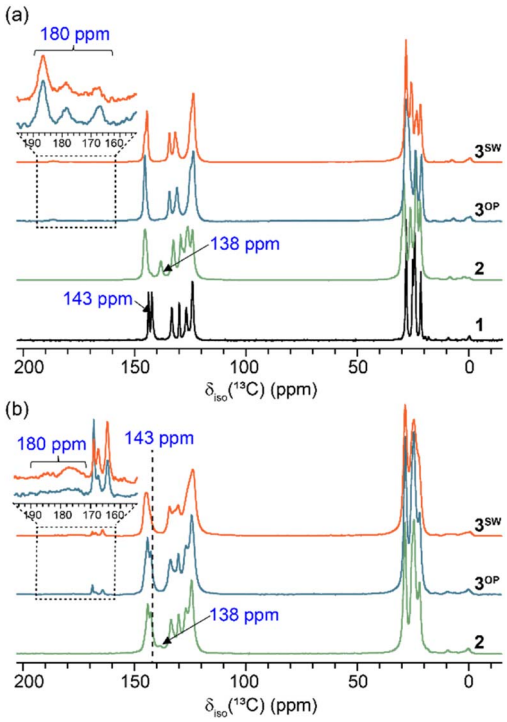

Fig. 2 1D ^{1}H → ^{13}C CP-MAS NMR spectra of (a) purified and (b) crude 2 (green), $\mathbf{3}^{OP}$ (blue), and $\mathbf{3}^{SW}$ (orange) samples acquired at B_0 = 9.4 T with ν_R = 12.5 kHz. The spectrum of the purified 1 is also shown in black in panel (a) for the sake of comparison. The multiplet assigned to the C2 site for samples $\mathbf{3}^{OP}$ and $\mathbf{3}^{SW}$ is shown as an inset in panels (a) and (b). The isotropic chemical shifts of the ^{13}C2 nucleus are indicated on the spectra. Furthermore, the vertical dashed line in panel (b) denotes the isotropic chemical shift of the ^{13}C2 nucleus in compound **1**.

purified sample but not in the crude (Fig. S3). However, by increasing the ball-milling time to 30 min, the cuprate H2 signal is also detected in the crude sample **2** (Fig. 1b), which confirms the formation of the cuprate in the solid-state during ball milling. The ^{1}H spectra of crude **2** and $\mathbf{3}^{OP/SW}$, depicted in Fig. 1b, exhibit a H2 signal resonating at 12.5 ppm, indicating the presence of unreacted IPr·HCl in the crude samples. In addition, a ^{1}H signal at 13.5 ppm attributed to $KHCO_3$ is present in the ^{1}H spectra of crude $\mathbf{3}^{OP/SW}$.[31]

^{13}C ssNMR spectroscopy. To confirm these observations, we also acquired ^{1}H → ^{13}C cross-polarization under MAS (CP-MAS) spectra of the same samples (Fig. 2). These spectra were assigned (see Fig. S4) based on ^{13}C isotropic chemical shifts measured in solution,[32,33] 2D ^{1}H–^{13}C HETCOR spectra with ^{1}H detection (^{1}H{^{13}C}) using double CP sequence (see Fig. S5),[34,35] and DFT calculations of ^{13}C isotropic chemical shifts for isolated molecules and periodic crystal structures (see Fig. S6 and Table S2). The 2D ^{1}H{^{13}C} HETCOR spectra were acquired at a high magnetic field (B_0 = 18.8 T) and high MAS frequency (ν_R = 60 kHz) to improve the resolution of ^{1}H dimension and using short contact times for the CP transfers to probe selectively the proximities between covalently bonded ^{1}H and ^{13}C nuclei. In particular, the observation in these 2D spectra of a cross peak between ^{1}H and ^{13}C signals at 12.5 and 143 ppm for compound **1** and at 10 and 138 ppm for purified compound **2** confirms that these ^{13}C signals are assigned to C^2 atoms. These 2D spectra also facilitate the assignment of ^{1}H and ^{13}C aromatic signals and those from positions 4 and 5. Fig. S6 also shows the good agreement between the experimental and DFT-calculated isotropic chemical shift values for **1** and purified compounds **2** and $\mathbf{3}^{OP}$.

The 1D ^{1}H → ^{13}C NMR spectra of compounds $\mathbf{3}^{OP}$ and $\mathbf{3}^{SW}$ also exhibit a multiplet around 180 ppm assigned to ^{13}C2 nuclei in [Cu(Cl)(IPr)]. This multiplet arises from *J*-coupling and second-order quadrupolar-dipolar cross-terms with ^{63,65}Cu isotopes with spin I = 3/2.[36,37] This interpretation is confirmed by smaller splitting at a higher magnetic field, as seen in Fig. 3, since the second-order quadrupolar-dipolar cross-terms are inversely proportional to the B_0 field strength. Assuming that the shortest C–Cu distance is equal to that measured by X-ray diffraction, 1.953 Å,[38] the ^{13}C–^{63,65}Cu dipolar coupling

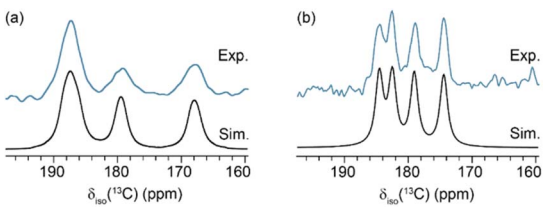

Fig. 3 Expansions of experimental (blue) and simulated (black) 1D^{13} C2 signals in 1D ^{1}H → ^{13}C CP-MAS NMR spectra of $\mathbf{3}^{OP}$ recorded at (a) B_0 = 9.4 T with ν_R = 12 kHz and (b) B_0 = 18.8 T with ν_R = 18 kHz.

constants are equal to $b(^{13}C–^{63}Cu)/(2\pi) = 0.93$ $b(^{13}C–^{65}Cu)/(2\pi) = 1.078$ kHz since the ratio of $^{63,65}Cu$ gyromagnetic ratios is $\gamma(^{63}Cu)/\gamma(^{65}Cu) = 0.93$. Using these dipolar coupling constants, these spectra can be simulated with $\delta_{iso} = 180$ ppm, the isotropic value of the indirect $^{13}C–^{63,65}Cu$ coupling tensor, $^1J_{iso}(^{13}C–^{63}Cu) = 0.93$ $^1J_{iso}(^{13}C–^{65}Cu) = 682 \pm 8$ Hz, its anisotropy, $\Delta^1J(^{13}C–^{63}Cu) = 0.93$ $\Delta^1J(^{13}C–^{65}Cu) = -160 \pm 260$ Hz and quadrupolar coupling constants, $C_Q(^{63}Cu) = 1.08$ $C_Q(^{65}Cu) = 80 \pm 5$ MHz since the ratio of electric quadrupolar moments of $^{63,65}Cu$ isotopes is $Q(^{63}Cu)/Q(^{65}Cu) = 1.08$. These parameters are close to those recently measured for [Cu(Cl)(NHC)] complex, in which the NHC ligand was *N*,*N*′-bis-[2,4,6-trimethylphenyl] imidazole-2-ylidene.[37,38] The best-fit $C_Q(^{63}Cu)$ value agrees well with that calculated using DFT from the periodic crystal structure of [Cu(Cl)(IPr)] (67 MHz). Its large value stems from a large electric field gradient owing to the highly asymmetric environment of the Cu atom in this compound. The measured $^1J_{iso}(^{13}C–^{63}Cu)$ coupling constant agrees with that calculated using DFT for the isolated [Cu(Cl)(IPr)] complex (660 Hz). Furthermore, the calculated $\Delta^1J(^{13}C–^{63}Cu)$ value of 112 Hz is consistent with experimental one given the high standard deviation in the measured $\Delta^1J(^{13}C–^{63}Cu)$ value.

As seen in Fig. 2b, the 1D $^1H \rightarrow ^{13}C$ CPMAS spectrum of crude 2 sample exhibits a peak at 138 ppm showing the formation of $[CuCl_2][IPr{\cdot}H]$ cuprate (**2**) in the solid state during the ball milling in agreement with ^1H NMR spectrum. The $^1H \rightarrow ^{13}C$ CPMAS spectra of crude $\mathbf{3^{OP/SW}}$ samples do not exhibit any signal at 138 ppm but a broad signal near 180 ppm. Furthermore, no cross peak between ^1H and ^{13}C signals at 10 and 138 ppm, respectively, is detected in their 2D $^1H\{^{13}C\}$ HETCOR spectra shown in Fig. S7b and c. This observation shows that during ball milling, the [Cu(Cl)(IPr)] complex is formed in the solid state, whereas the cuprate is totally transformed into this complex. The spectra of crude **2** and $\mathbf{3^{OP/SW}}$ samples also exhibit an additional signal at 143 ppm indicating the presence of unreacted IPr·HCl. Moreover, the signals at 162 and 169 ppm detected in the ^{13}C spectra of crude $\mathbf{3^{OP/SW}}$ indicate the presence of $KHCO_3$ and K_2CO_3, respectively.[31] The spectra of crude samples exhibit broader signals than those of purified samples owing to the disorder created by ball milling. The ^1H, ^{13}C and ^{15}N NMR resonances of pure $\mathbf{3^{SW}}$ compound are narrower than those of pure $\mathbf{3^{OP}}$ because the former is better crystallized than the latter. This line narrowing improves spectral resolution and allows the observation of additional peaks in the ^1H and $^1H \rightarrow ^{13}C$ spectra of pure $\mathbf{3^{SW}}$ shown in Fig. 1a and 2a, respectively.

This broadening is especially large for the C2 multiplet of [Cu(Cl)(IPr)] complex since the disorder results in a distribution of $C_Q(^{63,65}Cu)$ values, and hence, splitting due to second order quadrupolar-dipolar cross-terms.

For this initial part of the study, a clear mechanistic picture of the formation of [Cu(Cl)(NHC)] complexes was obtained. The ssNMR spectroscopic data along with DFT calculations of NMR parameters show unequivocally that the cuprate and the desired Cu–NHC complex are formed in the solid state during the ball milling event and not during workup when the crude reaction solids are in contact with solvent. Additionally, the cuprate intermediate is not detected in the crude samples of the final product, indicating the simultaneous conversion of cuprate into [Cu(Cl)(NHC)]. We have also shown that solid-state NMR can be used to assess the presence of unreacted reagents, such as NHC·HCl and K_2CO_3, as well as the formation of other reaction products, such as $KHCO_3$.

While the formation of cuprates has now been confirmed in the mechanochemical solid-state synthesis (as well as in solution, from our previous work on Cu, Au and Pd), our effort in identifying metalates in solution for rhodium systems have met with little success. A detailed examination of the solid-state transformation was initiated to understand the mechanism at play in the formation of Rh(I)–NHC complexes of the type [Rh(acac)(CO)(NHC)] (**5**), obtained from $[Rh(acac)(CO)_2]$ (**4**) (with acac = acetylacetonato) and an imidazolium salt (Scheme 4) with the goal of possibly observing rhodate intermediates.

The [Rh(acac)(CO)(L)] (L = two-electron-donor) complexes are obtained in a one-step ligand displacement reaction leading to the elimination of one CO ligand (Scheme 4A). Nolan[39] and more recently Carrow and co-workers[40] have exploited this class

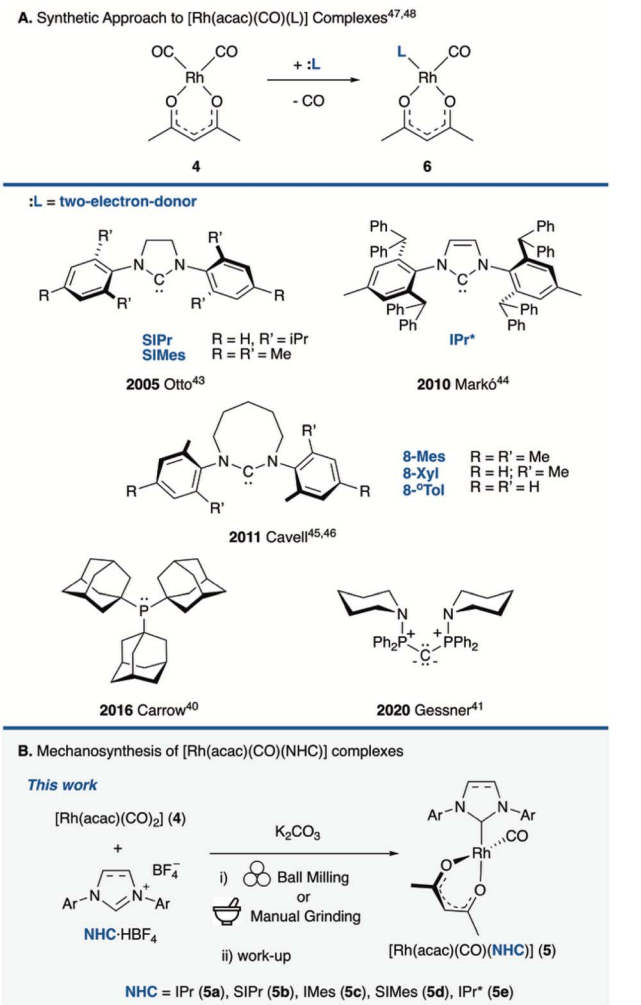

Scheme 4 (A). Synthetic approach to [Rh(acac)(CO)(L)] (**6**) complexes. (B) Mechanochemical synthesis of [Rh(acac)(CO)(NHC)] (**5**) complexes.

of complexes to assess the Tolman electronic parameter (TEP) of ligands through linear correlation analysis involving the carbonyl stretching frequency found in [Rh(acac)(CO)(PR_3)] complexes and the TEP values (from $Ni(CO)_3L$) for this same set of phosphine ligands.[39,40] Using the same linear correlation analysis, Gessner and co-workers have assessed the TEP value for a di(amino)-substituted carbodiphosphorane (CDP) ligand by recording the IR stretching frequency in the corresponding [Rh(acac)(CO)(L)] (**6**).[41] Recently, Cazin has used such complexes as electrochemical probes to assess ligand electronic properties, enabling direct correlation of ν_{CO} and $E_{1/2}$.[42] This class of complexes has undoubtedly become an interesting platform to assess ligand electronic properties.

All [Rh(acac)(CO)(NHC)] (**5**) complexes reported to date[42–48] have been obtained through synthetic routes that require strictly anhydrous conditions. While we have recently disclosed a solvent-based synthetic protocol that allows for the assembly of these complexes using operationally simple conditions and readily available starting materials,[42,48] this solvent-based method is marked by relatively long reaction times (ranging from 3 to 18 hours, depending on the nature of the NHC·HBF_4 salt employed) at high temperatures. This is in striking contrast with the reaction time needed when reactions are carried out in solid-state. Indeed, when we investigated the feasibility of the reaction under mechanochemical conditions, we found that 30 minutes of grinding were sufficient for the assembly of a series of *N*,*N*′-diaryl NHC–Rh(I) complexes of the type [Rh(acac)(CO)(NHC)] (**5**). Initial experiments were carried out using *N*,*N*′-bis-[(2,6-di(isopropylphenyl)]imidazolium, (IPr·HBF_4), an excess of K_2CO_3, and [Rh(acac)$(CO)_2$] (**4**) (Scheme 4B). Note that the BF_4 salt was used instead of the imidazolium chloride in view of the hygroscopic nature of the latter and the water resistance and high stability, crystallinity of the former. The reaction (as were subsequent others) was carried out in a planetary ball mill, using a ZrO_2 reactor charged with 28 ZrO_2 balls (10.3 g, $\varnothing = 5$ mm, corresponding to a filling degree for the milling bodies of $\Phi_{MB} = 0.15$) on a 100 mg scale of the NHC·HBF_4 salt. Gratifyingly, these conditions resulted in the formation of the desired complex.[49] An intriguing feature of this reaction was the colour change of the solid reagents throughout the process up to the final desired product (Scheme 5). When [Rh(acac)$(CO)_2$] (**4**), which displays a pronounced dichroic character (appearing green by diffraction and red in transmission),[50] was milled with IPr·HBF_4 and an excess of K_2CO_3, the solids were converted to a red amaranth powder (**5a***) which affords the desired [Rh(acac)(CO)(IPr)] complex (**5a**) as a yellow powder after workup. This last colour change occurs spontaneously upon extraction of **5a*** from the reactor using a solvent, this with concomitant gas evolution (Scheme 5). To confirm the identity of the gas, an experiment was carried out in a Landolt tube (Scheme S1), with the first tube charged with the milled solids mixture **5a*** and the second chamber loaded with a solution of [Ir(Cl)(COD)(IPr)] **7**.

Addition of solvent to the first chamber resulted in vigorous frothing/gas evolution which led to reaction with **7** in the second chamber and to formation of [Ir(Cl)$(CO)_2$(IPr)] (**8**).[51] This unequivocally confirms that CO(g) is the gas released upon solvent addition in the first chamber (see SI for details). This observation suggests that the workup itself is key to product formation.

Considering these data, the necessity for the mechanical treatment prior to reaction was questioned and was determined by recording the kinetic profiles (*in situ* IR monitoring) of reactions carried out in solution using the pre-ground solids (**5a***) and the unground solids. These experiments show the exceptional effect of the pre-grinding, leading to reaction completion within a few minutes, while the same reaction carried out with non-pre-ground material requires several hours at room temperature.[52] Fig. 4 shows the profile obtained with the IPr derivative. This effect of the pre-grinding on reaction rate is even more striking when the bulkier congener IPr* is used (SI Fig. S40), with which the reaction using pre-ground starting materials is essentially instantaneous upon solvent addition, while the same reaction carried with non-pre-ground starting material is very sluggish. In addition, we observed that pre-grinding the base alone also increases reaction rate,

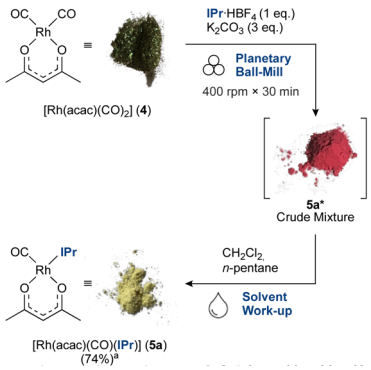

Scheme 5 Mechanochemical synthesis of [Rh(acac)(CO)(IPr)] (**5a**). Reaction conditions: (i) IPr·HBF_4 (100 mg, 0.21 mmol), [Rh(acac)$(CO)_2$] (**4**) (54 mg, 0.21 mmol), K_2CO_3 (87 mg, 0.63 mmol), planetary ball mill, 400 rpm, 30 min. (ii) Solvent workup. [a] Isolated yield.

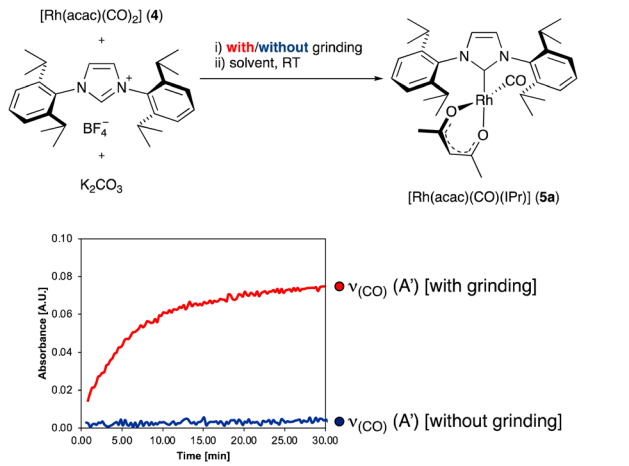

Fig. 4 Kinetic profiles of reactions with starting material pre-ground (red); not ground (blue). *In situ* IR monitoring of ν_{CO} product (1961 cm^{-1}).

but not as drastically as when all reactants are pre-ground together. We therefore note that particle size but also mixing of the solids have an important influence on the reaction kinetics. We next examined whether such results could also be achieved with manual grinding using simple mortar and pestle. As shown in Scheme 6, this is indeed the case, as after manually pre-grinding the components of the reaction, followed by solvent addition/workup, a 72% yield of the Rh–NHC complex was isolated.

To obtain experimental evidence as to the exact identity of the solids obtained after milling and to offer insights into how this reaction does indeed proceed, we investigated the nature of the crude reaction mixture without resorting to analytical methods that require prior dissolution of solids in a liquid medium.

ATR-FTIR (Attenuated total reflectance Fourier transform infrared) spectroscopic analyses were performed directly on the solids of the crude reaction mixture **5a***, the [Rh(acac)(CO)$_2$] **4**, and the [Rh(acac)(CO)(IPr)] final product **5a**. The fingerprint infrared carbonyl region unambiguously establishes that no significant differences exist between the spectrum of [Rh(acac)(CO)$_2$] **4** and the one of the resulting solid **5*** after milling. The CO stretching frequencies related to the A_1 and B_1 vibrational modes are present in both spectra but are slightly shifted. Upon workup of the milled solids using solvents, clear conversion to [Rh(acac)(CO)(IPr)] **5a** is observed, with a single CO band appearing at 1958 cm^{-1} (Fig. 5).

These pre-ground solids were then studied using solid-state NMR spectroscopy (Fig. 6). The 1D ^{1}H NMR spectra of these solids were recorded under MAS with the homonuclear dipolar decoupling scheme wDUMBO[53] to enhance spectral resolution (Fig. 6B). The spectral assignments are given in Fig. S11 (see SI). The ^{1}H spectrum of reaction mixture **5a*** contains signals of the reactants, IPr·HBF$_4$ and **4**, but does not display those of the final product **5a**. Similar conclusions were reached from ^{13}C NMR spectra acquired using ^{1}H → ^{13}C cross-polarization under MAS (CPMAS) sequence (see Fig. 6A and assignment given in Fig. S12).

Specifically, the ^{13}C spectrum of **5a*** does not exhibit a doublet at 192 ppm, corresponding to the ^{13}C2 signal of the imidazolylidene moiety in the final product **5a**. Conversely, the spectrum of this compound contains a singlet at 140 ppm assigned to the ^{13}C2 signal of IPr·HBF$_4$. Furthermore, the carbonyl ^{13}C signals are similar for solids **4** and **5a*** and differ from those of **5a**. In particular, the ^{13}C signal of the CO ligand of

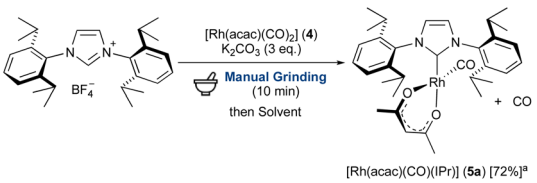

Scheme 6 Synthesis of [Rh(acac)(CO)(IPr)] (**5a**) using manual grinding. Conditions: IPr·HBF$_4$ (100 mg, 0.21 mmol), [Rh(acac)(CO)$_2$] (**4**) (54 mg, 0.21 mmol), and K$_2$CO$_3$ (87 mg, 0.63 mmol), in a mortar and pestle with grinding time of 10 min. [a] Isolated yield after workup involving solvent.

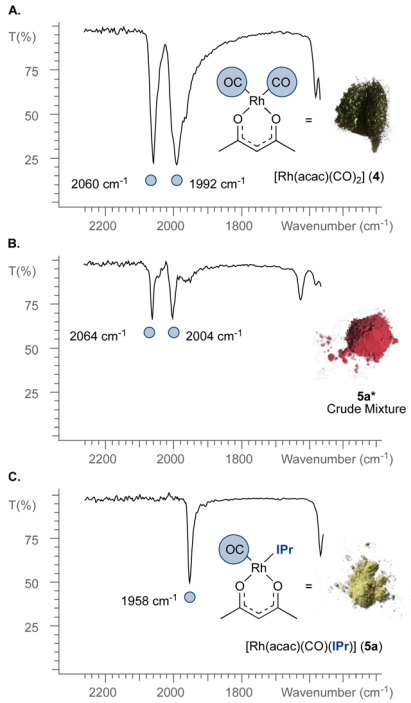

Fig. 5 ATR-FTIR spectra of solids [carbonyl stretching frequencies region] for: (A) [Rh(acac)(CO)$_2$] **4**; (B) the crude reaction mixture **5a***; (C) [Rh(acac)(CO)(IPr)] **5a**.

5a at 178 ppm is not observed in the spectrum of **5a***. The signal at 170 ppm in the ^{13}C spectrum of **5a*** also indicates the presence of K$_2$CO$_3$.[21] Hence, the crude mixture contains unreacted **4**, IPr·HBF$_4$, and K$_2$CO$_3$ but no final product **5a**.

The 1D ^{1}H → ^{15}N CPMAS, ^{11}B, and ^{19}F MAS spectra, shown in Fig. 6C–E, respectively, further confirm the presence of IPr·HBF$_4$ in the crude mixture and the absence of **5a**. The ^{19}F signal of IPr·HBF$_4$ is broadened in the **5a*** mixture with respect to the pure reagent. This broadening indicates a distribution of the local environment of ^{19}F nuclei in **5a*** mixture arising from the creation of crystallographic defects or reactant mixing by ball milling. In addition, the ^{15}N signal at 184 ppm is identical to that of IPr·HBF$_4$. This result is consistent with the ^{1}H and ^{13}C data and supports our initial suspicion that **5a** is not formed during the ball milling event but is formed only after the workup of the milled solids upon solvent addition.

The powder XRD pattern of **5a*** (see SI Fig. S13) shows that this mixture contains **4**, IPr·HBF$_4$ and K$_2$CO$_3$ crystallites. Furthermore, reflections from **5a** crystals were not detected in the XRD pattern of **5a***. This observation confirms that the final complex is not formed before the addition of the solvent. The reflections of **5a*** powder pattern are broader than those of the reagents since ball milling reduces the size of the crystallites and results in the formation of crystallographic defects (Fig. S14). Therefore, all experimental data collected show that **5a*** is a physical mixture of the reagents resulting from mechanical treatment. When the solids are treated with various solvents, product **5a** is smoothly formed with concomitant gas evolution (Fig. S15).

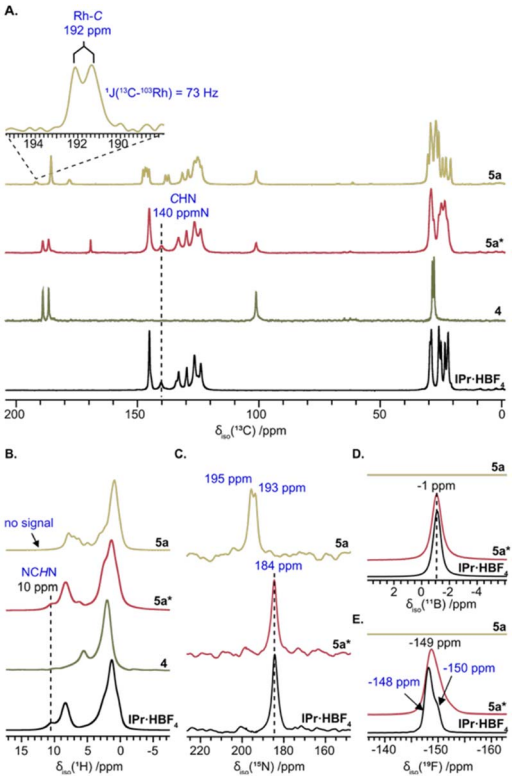

Fig. 6 (A) 1D $^{1}H \rightarrow {}^{13}C$ CPMAS, (B) ^{1}H wDUMBO-decoupled, (C) $^{1}H \rightarrow {}^{15}N$ CPMAS, (D) ^{11}B and (E) ^{19}F MAS NMR spectra of IPr·HBF_4 (black), [Rh(acac)$(CO)_2$] (**4**) (green), the crude reaction mixture (**5a***) (red) and [Rh(acac)(CO)(IPr)] (**5a**) complex (olive) acquired at 9.4 T with a MAS frequency of 12.5 kHz. An expansion of the $^{1}H \rightarrow {}^{13}C$ CPMAS spectrum of (**5a**) showed as an inset in panel A displays the doublet assigned to the $^{13}C2$ nucleus of the imidazolylidene ring split by the *J*-coupling constant $^{1}J(^{13}C-^{103}Rh) = 73$ Hz.

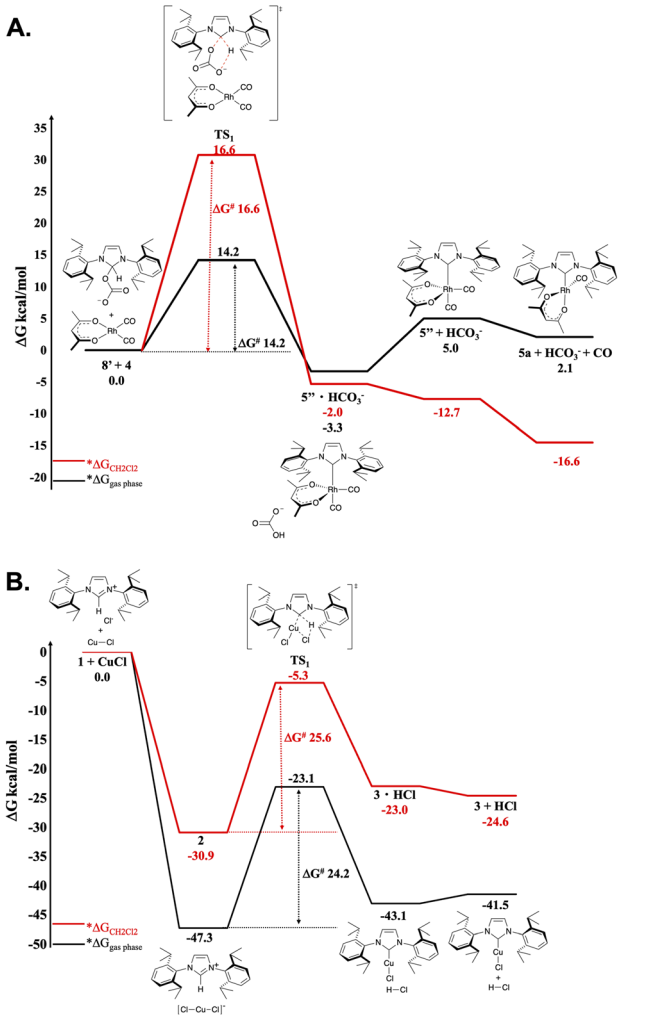

Fig. 7 (A). Computed reaction pathways from **8′** and **4** to **5a**. Values reported are Δ*G* in the gas phase (black values) and in CH_2Cl_2 (red values) in kcal mol^{-1}.[54,55] (B). Computed reaction pathway from **1** to **2** and finally to **3** in solution (red values) and in the gas phase (black values) in kcal mol^{-1}.

Computational studies (DFT) were conducted to gain further insights into the thermodynamics of this process, intermediates, and transition states (TSs) involved in the reaction of IPr·HBF_4 with **4** in the presence of K_2CO_3 to form **5a**. As **5a** corresponds experimentally to a heterogeneous physical mixture of solid components and is therefore not directly amenable to molecular DFT treatment, calculations were performed starting from the product of the addition of $[IPr \cdot H]^+$ and CO_3^{2-}, namely $[IPr \cdot HCO_3]^-$ (**8′**), and the Rh complex (**4**) at infinite distance, which was set as zero energy.

Fig. 7A presents the free energy changes resulting from calculations in the gas phase (values in black) and in CH_2Cl_2 as the solvent (values in red). From (**8′**) the hydrogen of $[IPr \cdot H]^+$ is transferred to CO_3^{2-} forming HCO_3^- species through a transition state (TS) at +14.2 and +16.6 kcal mol^{-1}, in the gas phase and in CH_2Cl_2, respectively. In this TS, the rhodium complex interacts with the oxygen of the CO_3^{2-} through the hydrogen of the methyl group of the acac ligand (see Fig. 8A), resulting in a small stabilization effect (see Fig. S16).

Moving forward, deprotonation of IPr in the TS results in its spontaneous coordination to the rhodium complex, generating a kinetic product (**5″**·HCO_3^-), at −3.3 kcal mol^{-1} in the gas phase and at −2.0 kcal mol^{-1} in CH_2Cl_2 in which a pentacoordinate species (**5″**) is stabilized by the interaction of one acac oxygen atom with the proton of the non-coordinating HCO_3^- anion (see Fig. 8B). Finally, the pentacoordinate intermediate (**5″**·HCO_3^-) evolves by HCO_3^- and CO elimination to

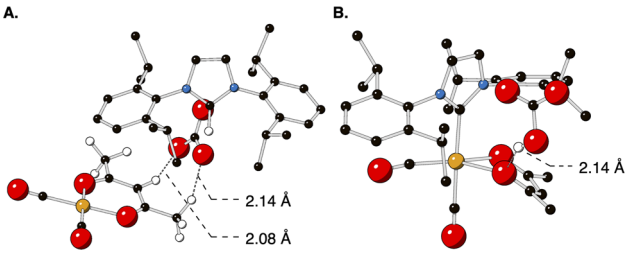

Fig. 8 Geometries of: (A) transition state (TS) and (B) the kinetic product of the pentacoordinate intermediate (**8″**·HCO_3^-) with HCO_3^- anion interaction with acac ligand.

the product (**5a**), which is energetically favoured only in a solvent (+2.1 kcal mol^{-1} in gas phase and −16.6 kcal mol^{-1} in CH_2Cl_2). This difference is attributed to solvent stabilization of the leaving HCO_3^- anion, while CO dissociation is essentially thermoneutral.

Comparison of the vibrational frequencies of the CO groups in our intermediates with the experimental data (Fig. S17) clearly shows that the CO stretching frequencies found in our intermediate spectra are comparable with the experimentally found frequencies.

To address the energetics of the mechanochemical reaction in the copper system, a similar profile was calculated (see Fig. 7B). Calculations clearly show that the initial interaction between IPr·HCl and CuCl is remarkably exergonic. This favourable interaction drives the reaction to overall negative free energies along the entire reaction pathway, both in gas-phase and solvent simulations. These computational results align well with the experimental formation of **3**, observed in both the gas-phase and in solution.

In grinding experiments conducted with both a mixer mill and a planetary orbital shaker under liquid assisted grinding (LAG), product **5a** was formed after grinding, without the need for any workup. For details and IR spectra, see SI Fig. S48 and S49. Temperature (external or during grinding) may also contribute to product formation. Using either milling instruments identical results were obtained where **5a** is not formed. However, heating ground samples permits some product formation at temperatures of 120 °C as evidenced by FT-IR ATR spectroscopy in the solid state (Fig. S50 and S51).

Conclusion

The mechanisms leading to the formation of [Cu(NHC)Cl] and [Rh(acac)(CO)(NHC)] complexes were examined through a combination of spectroscopic and computational means. These methods permit to confirm that for the Cu system, the chemical transformation is achieved during milling/grinding. However, for the rhodium system, the need for solvent is evident to bring the ligand binding/substitution event to completion and to product formation for the Rh system, but milling/grinding assists the reaction but the drive towards product is brought about by events occurring upon or after solvent addition for the Rh system. Particle size and mixing affect solution reaction kinetics. The results for the Rh system are somewhat unexpected, but the described method and observations should prove convenient to the community for synthetic access to organometallic complexes and might be applicable to other systems obtained through mechanochemical means. The pre-grinding/milling effect can be of significant practical use to accelerate reaction kinetics.

As a closing remark, the two systems studied clearly show that there is no single reaction mechanism involved in mechanosynthesis. This may not come as a surprise to the practitioners of physical organometallic chemistry but here, we show that reaction or conversion can occur during or post mechanochemical grinding. The evolution of a gas during the reaction favours product formation and this entropic factor may be crucial in dictating the mechanistic route by which mechanochemical reactions proceed. This study may also serve as a caveat to those making common use of mechanochemical synthesis in highlighting that each system can be unique in possessing given thermodynamic driving forces (entropic and enthalpic) and that these should be considered before proposing (or assuming) mechanochemical reaction mechanisms.

Author contributions

GP, LH, JT, OD, AGMR and PR carried out experimental work and contributed to the writing of the manuscript. IR, LF, LD and LC conducted computational work and contributed to the writing of the manuscript. OL, LC, SPN and CSJC conceived and supervised the work, secured funding, and contributed to the writing and editing of the manuscript.

Conflicts of interest

There are no conflicts to declare.

Data availability

The data supporting this article have been included as part of the supplementary Information (SI). Supplementary information is available. See DOI: https://doi.org/10.1039/d6sc01038e.

Acknowledgements

We gratefully acknowledge the Special Research Found (BOF) of Ghent University. The Chevreul Institute (FR 2638), Ministère de l'Enseignement Supérieur de la Recherche et de l'Innovation, Hauts-de-France Région, IR Infranalytics (FR 2054) and FEDER are acknowledged. This project has received funding from the European Union Horizon 2020 research and innovation program under the Skłodowska-Curie agreement No. 847568. Umicore AG and Johnson Matthey are gratefully acknowledged for gifts of materials. Gianluca Carí is thanked for conducting the LAG and high temperature experiments. We thank the reviewers for helpful suggestions.

Notes and references

1 J. L. Do and T. Friščić, *ACS Central Sci.*, 2017, **3**, 13–19.
2 T. Friščić and H. M. Titi, *Angew. Chem., Int. Ed.*, 2020, **59**, 1018–1029.
3 A. Stolle, T. Szuppa, S. E. S. Leonhardt and B. Ondruschka, *Chem. Soc. Rev.*, 2011, **40**, 2317–2329.
4 D. Tan and T. Friščić, *Eur. J. Org Chem.*, 2018, **2018**, 18–33.
5 N. R. Rightmire and T. P. Hanusa, *Dalton Trans.*, 2016, **45**, 2352–2362.
6 A. Beillard, X. Bantreil, T. X. Métro, J. Martinez and F. Lamaty, *Chem. Rev.*, 2019, **119**, 7529–7609.
7 D. Tan and F. Garcia, *Chem. Soc. Rev.*, 2019, **48**, 2274–2292.
8 T. Friščić, *Chem. Soc. Rev.*, 2012, **41**, 3493–3510.

9 A. Porcheddu, E. Colacino, L. De Luca and F. Delogu, *ACS Catal.*, 2020, **10**, 8344–8394.
10 C. Bolm and J. G. Hernandez, *ChemSusChem*, 2018, **11**, 1410–1420.
11 C. J. Clarke, W.-C. Tu, O. Levers, A. Bröhl and J. P. Hallett, *Chem. Rev.*, 2018, **118**, 747–800.
12 J. L. Howard, Q. Cao and D. L. Browne, *Chem. Sci.*, 2018, **9**, 3080–3094.
13 J. G. Hernandez and C. Bolm, *J. Org. Chem.*, 2017, **82**, 4007–4019.
14 For a recent example, see:T. Seo, N. Toyoshima, K. Kubota and H. Ito, *J. Am. Chem. Soc.*, 2021, **143**, 6165–6175.
15 G. Kaupp, *CrystEngComm*, 2009, **11**, 388–403.
16 E. Boldyreva, *Chem. Soc. Rev.*, 2013, **42**, 7719–7738.
17 R. F. Koby, A. M. Doerr, N. R. Rightmire, N. D. Schley, W. W. Brennessel, B. K. Long and T. P. Hanusa, *Chem. Eur. J.*, 2021, **27**, 8195–8202.
18 S. Lukin, L. S. Germann, T. Friščić and I. Halasz, *Acc. Chem. Res.*, 2022, **55**, 1262–1277.
19 J. G. Schiffmann, F. Emmerling, I. C. B. Martins and L. Van Wüllen, *Solid State Nucl. Magn. Res.*, 2020, **109**, 101687.
20 S. Gupta, T. Kobayashi, J. F. Goldston and V. K. Pecharsky, *Green Chem.*, 2014, **16**, 4378–4388.
21 Y. Xu, L. Champion, B. Gabidullin and D. L. Bryce, *Chem. Commun.*, 2017, **53**, 9930–9933.
22 S. Kaabel, R. S. Stein, M. Fomitšenko, I. Järving, T. Friščić and R. Aav, *Angew. Chem., Int. Ed.*, 2019, **58**, 6230–6234.
23 I. d'Anciães Almeida Silva, E. Bartalucci, C. Bolm and T. Wiegand, *Adv. Mat.*, 2023, **35**, 2304092.
24 E. A. Martynova, N. V. Tzouras, G. Pisanò, C. S. J. Cazin and S. P. Nolan, *Chem. Commun.*, 2021, **57**, 3836–3856.
25 S. De, F. Joó, H. Horváth, A. Udvardy and C. E. Czégéni, *J. Organomet. Chem.*, 2020, **918**, 121308.
26 G. Pisanò and C. S. J. Cazin, *Green Chem.*, 2020, **22**, 5253–5256.
27 G. Pisanò and C. S. J. Cazin, *ACS Sustainable Chem. Eng.*, 2021, **9**, 9625–9631.
28 Q. Liao, K. Su, H. Cai, T. Zhao and F. Liu, *J. CO_2 Util.*, 2022, **59**, 101963.
29 N. V. Tzouras, F. Nahra, L. Falivene, L. Cavallo, M. Saab, K. Van Hecke, A. Collado, C. J. Collett, A. D. Smith, C. S. J. Cazin and S. P. Nolan, *Chem. Eur. J.*, 2020, **26**, 4515–4519.
30 K. J. Ardila-Fiero and J. G. Hernández, *Angew. Chem., Int. Ed.*, 2024, **63**, e202317638.
31 D. Stueber, D. Patterson, C. L. Mayne, A. M. Orendt, D. M. Grant and R. W. Parry, *Inorg. Chem.*, 2001, **40**, 1902–1911.
32 O. Santoro, A. Collado, A. M. Z. Slawin, S. P. Nolan and C. S. J. Cazin, *Chem. Commun.*, 2013, **49**, 10483–10485.
33 A. Beillard, T.-X. Métro, X. Bantreil, J. Martinez and F. Lamaty, *Chem. Sci.*, 2017, **8**, 1086–1089.
34 Y. Ishii, J. P. Yesinowski and R. Tycko, *J. Am. Chem. Soc.*, 2001, **123**, 2921–2922.
35 J. W. Wiench, C. E. Bronnimann, V. S.-Y. Lin and M. Pruski, *J. Am. Chem. Soc.*, 2007, **129**, 12076–12077.
36 R. K. Harris and A. C. Olivieri, *Prog. Nucl. Magn. Reson. Spectrosc.*, 1992, **24**, 435–456.
37 N. Kaeffer, D. Mance and C. Copéret, *Angew. Chem., Int. Ed.*, 2020, **132**, 20174–20182.
38 H. Kaur, F. K. Zinn, E. D. Stevens and S. P. Nolan, *Organometallics*, 2004, **23**, 1157–1160.
39 S. A. Serron, J. Huang and S. P. Nolan, *Organometallics*, 1998, **17**, 534–539.
40 L. Chen, P. Ren and B. P. Carrow, *J. Am. Chem. Soc.*, 2016, **138**, 6392–6395.
41 A. Kroll, H. Steinert, L. T. Scharf, T. Scherpf, B. Mallick and V. H. Gessner, *Chem. Commun.*, 2020, **56**, 8051–8054.
42 F. Bru, R. S. C. Charman, L. Bourda, K. Van Hecke, L. Grimaud, D. J. Liptrot and C. S. J. Cazin, *Dalton Trans.*, 2024, **53**, 16030–16037.
43 M. S. Datt, J. J. Nair and S. Otto, *J. Organomet. Chem.*, 2005, **690**, 3422–3426.
44 G. Berthon-Gelloz, M. A. Siegler, A. L. Spek, B. Tinant, J. N. Reek and I. E. Marko, *Dalton Trans.*, 2010, **39**, 1444–1446.
45 M. Iglesias, D. J. Beetstra, K. J. Cavell, A. Deryisi, I. A. Fallis, B. Kariuki, R. W. Harrington, W. Clegg, P. N. Horton, S. J. Coles and M. B. Hursthouse, *Eur. J. Inorg. Chem.*, 2010, **2010**, 1604–1607.
46 W. Y. Lu, K. J. Cavell, J. S. Wixey and B. Kariuki, *Organometallics*, 2011, **30**, 5649–5655.
47 Q. Zhao, G. Meng, G. Li, R. Mendelsohn, R. Lalancette, R. Szostak and M. Szostak, *Chem. Sci.*, 2021, **12**, 10583–10589.
48 S. G. Guillet, G. Pisanò, S. Chakrabortty, B. H. Müller, J. G. de Vries, P. C. J. Kamer, C. S. J. Cazin and S. P. Nolan, *Eur. J. Inorg. Chem.*, 2021, **43**, 3506–3511.
49 Milling of other NHC salts used as reactants in this transformation for 30 min at 400 rpm afforded the desired metal complexes (**5a–5e**) in good to excellent isolated yields (see SI for details).
50 F. Bonati and G. Wilkinson, *J. Chem. Soc.*, 1964, 3156–3160.
51 R. A. Kelly, III, H. Clavier, S. Guidice, N. M. Scott, E. D. Stevens, J. Bordner, I. Samardjiev, C. D. Hoff, L. Cavallo and S. P. Nolan, *Organometallics*, 2008, **27**, 202–210.
52 For grinding effects in mechanochemical reactions, see: J. Templ and L. Borchardt, *Angew. Chem., Int. Ed.*, 2026, **65**, e23191.
53 S. Paul, R. S. Thakur, M. Goswami, A. C. Sauerweim, S. Mamone, M. Concistré, H. Förster, M. H. Levitt and P. K. Madhu, *J. Mag. Reson.*, 2009, **197**, 14–19.
54 Geometries were optimized with Gaussian09 package at the PBE0-D3 level of theory. The valence triple-zeta with two sets of polarization functions (Def2TZVPP) was used for Rh, Cu, H, C, N, Cl and O atoms. In gas phase, the reported free energies have been obtained considering the thermal free energies. Instead, the solvent energy profile has been computed adding the thermal corrections in gas-phase to the electronic energy in solvent (PCM model) calculated via single point energy calculations in CH2Cl2 with Def2TZVPP basis set for metal and main group atoms and

the triple-z with two sets of polarization functions and a set of diffuse functions (Def2TZVPPD) on one of the three oxygen atoms of the weak base and on Cl atoms.

55 M. J. Frisch, G. W. Trucks, H. B. Schlegel, G. E. Scuseria, M. A. Robb, J. R. Cheeseman, G. Scalmani, V. Barone, B. Mennucci, G. A. Petersson, H. Nakatsuji, M. Caricato, X. Li, H. P. Hratchian, A. F. Izmaylov, J. Bloino, G. Zheng, J. L. Sonnenberg, M. Hada, M. Ehara, K. Toyota, R. Fukuda, J. Hasegawa, M. Ishida, T. Nakajima, Y. Honda, O. Kitao, H. Nakai, T. Vreven, J. A. Montgomery, J. E. Peralta, F. Ogliaro, M. Bearpark, J. J. Heyd, E. Brothers, K. N. Kudin, V. N. Staroverov, R. Kobayashi, J. Normand, K. Raghavachari, A. Rendell, J. C. Burant, S. S. Iyengar, J. Tomasi, M. Cossi, N. Rega, J. M. Millam, M. Klene, J. E. Knox, J. B. Cross, V. Bakken, C. Adamo, J. Jaramillo, R. Gomperts, R. E. Stratmann, O. Yazyev, A. J. Austin, R. Cammi, C. Pomelli, J. W. Ochterski, R. L. Martin, K. Morokuma, V. G. Zakrzewski, G. A. Voth, P. Salvador, J. J. Dannenberg, S. Dapprich, A. D. Daniels, Ö. Farkas, J. B. Foresman, J. V. Ortiz, J. Cioslowski, and D. J. Fox, *Gaussian09 Revision D.01*, Gaussian Inc., Wallingford CT, 2009.